Soft Matter

Accepted Manuscript

ROYAL SOCIETY OF CHEMISTRY

www.rsc.org/softmatter

Disclination Elastica Model of Loop Collision and Growth in Confined Nematic Liquid Crystals

Alireza Shams[a], *Xuxia Yao*[b], *Jung Ok Park*[b,c], *Mohan Srinivasarao*[b,c,d] *and Alejandro D. Rey*[a*]

[a] Department of Chemical Engineering, McGill University, Montreal, Quebec H3A 0C5, Canada

[b] School of Materials Science and Engineering, Georgia Institute of Technology, Atlanta, GA 30332, USA

[c] Center for Advanced Research on Optical Microscopy, Georgia Institute of Technology, Atlanta, GA 30332, USA

[d] School of Chemistry and Biochemistry, Georgia Institute of Technology, Atlanta, GA 30332, USA

* Corresponding author: alejandro.rey@mcgill.ca

TABLE OF CONTENTS FIGURE

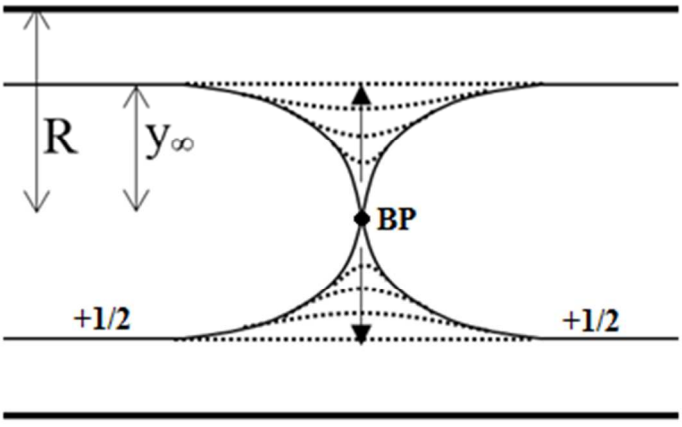

Keywords: *Disclinationelastica, confinement, Rouse-Frank model, defect physics.*

Abstract

Theory and modeling are used to characterize disclination loop-loop interactions innematic liquid crystals under capillary confinement with strong homeotropic anchoring. This defect process arises when quenching a mesogen in the isotropic phase into the stable nematic state. The texture evolution starts with +1/2 disclination loops that merge into a single loop through a process that involves collision, pinching and relaxation. The process is characterized with a combined Rouse-Frank model that incorporates the tension and bending elasticity of disclinations and the rotational viscosity of nematics. The Frank model of disclinations follows the Euler elastica model, whose non-periodic solution, known as Poleni's curve is shown to describe locally the loop-loop collision and to shed light on why loop-loop merging results in a disclination intersection angle of approximately 60°. Additional Poleni invariants demonstrate how tension and bending pinch the two loops into a single +1/2 disclination ring. The Rouse model of disclination relaxation yields a Cahn-Hilliard equation whose time constant combines confinement, tension/bending stiffness ratio and disclination diffusivity. Based on the three stage process predictions, a practical procedure is proposed to find viscoelastic parameters from defect geometry and defect dynamics. These finding contribute to the evolving understanding of textural transformations in nematic liquid crystals under confinement using the disclination elastica methodology.

1. Introduction

Nematic liquid crystals (NLCs) are anisotropic viscoelastic materials that possess long range macroscopic orientational order characterized by the unit director vector **n=-n**[1-2].Singular and non-singular orientational defects are generated by phase transitions, external electromagnetic fields, shear flows, and strong confinement.[1-13] Defects in nematic liquid crystals include point defects (0D), disclinations lines (1D) and inversion walls (2D).[1,14] A disclination line is characterized by a quantized charge *m* which presents the amount of rotation when encircling the line and the sign (+/-) associated with the charge denotes the sense of rotation.[2] Since the disclination energy per unit length scales with m^2, ±½ lines are energetically preferred.[2,9] Disclination evolution in nematic liquid crystals under confinement is a subject of continuing interest since frustration emanating from fixed orientation at curved bounding surfaces is a common phenomenon in various processes.[15-18] Since the structure and dynamics of disclinations is a function of local viscoelastic properties,[15] controlled defect nucleation and evolution in capillaries can serve to assess material moduli in a simple way. Compared to traditional methods to estimate viscoelastic properties including the Frederiks transition based on reorientation of the axis of nematic director by an applied field and light scattering on thermal fluctuations of the director,[19] the combined theoretical model and observed texture/defect data is simpler and cost effective. In this paper we focus on +1/2 disclination loop-loop collision, pinching and relaxation inside capillary tubes using the "*disclination elastica*" shape equation[7-10] that uses the Frank elastic free energy to define the line tension and line bending moduli and analysing Poleni's curve.[20]

The elastic problem was first posed by mathematician Jordan de Nemore in the thirteen century. In 1638 Galilieo did a mathematical study of elasticity by considering a prismatic beam set into wall at one end, and loaded by a weight at the other. Hooke presented his famous law in 1678 in which the applied force on a fiber is proportional to the change in length. Another elastic problem has published by James Bernoulli in 1691 and then Daniel Bernoulli proposes his variantional techniques in 1742. In 1744, Leonard Euler completely characterized the family of curves known as the elastica and proposed his famous equation for estimating of the energy of a curve.[21] The equation for the shape of the capillary was investigated by Pierre Simon Laplace in 1807 and in 1859 Kirchhoff showed the differential equations for elastic in form of curvature as a function of arc-length are equivalent to those of the motion of the pendulum.[21] Finally distortion free energy density equation which describes the increase in the free energy density of a liquid crystal caused by distortions and defects from its uniformly aligned configuration was published by Frederick Charles Frank in the twentieth century.[22] Our new model, nematic-elastica, has been derived based on the Euler equation and Frank elasticity model.

Here we briefly describe the controlled setting that gives rise loop-loop interactions that forms the basis of texture transformations in the nematic phase of chromonic liquid crystals.[11] Quenching an isotropic solution into a nematic state under strong homeotropic anchoring in a micron-range capillary gives rise to a planar radial (PR) texture with an axial +1 singular line. Due to the large m, the unstable line decays by a nucleation and growth process involving +1/2 disclination loops attached to the original +1 line through an isotropic branch point (BP) that satisfies Kirchhoff branching law.[7] Figure 1 shows two interacting + ½ loops attached to a shrinking +1 string inside a capillary of radius R; before collision (I) the loops have a ribbon

shape of width $2y_\infty = 1.33R$ with semicircular ends. At the collision stage (II), the loops merge and the two branch points fuse and form an unstable junction. Tension forces from the +1/2 lines pinch the junction (III, V), allowing the relaxation and formation of a single +1/2 large loop. The collision and coarsening of the larger +1/2 loops eventually lead to the formation of the planar polar (PP) texture with two parallel +1/2 lines separated by a distance $2y_\infty$=1.33R (IV).[23]

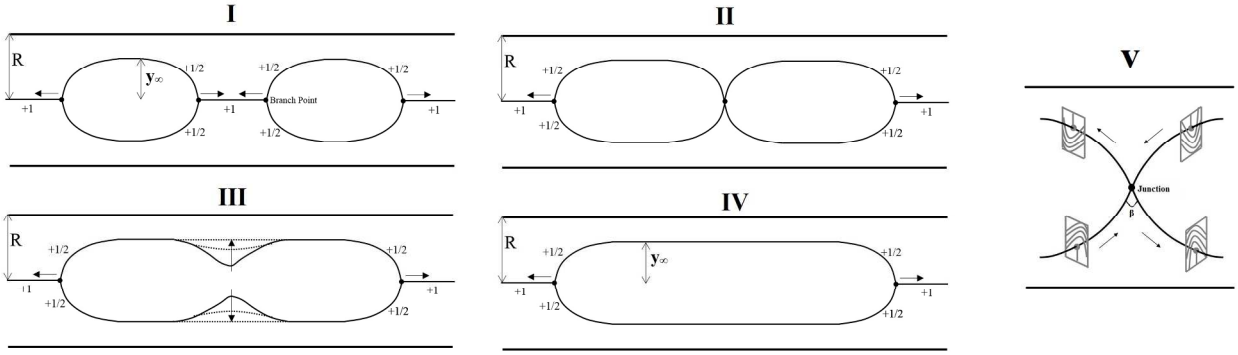

Figure 1. Collision and relaxation process of two+1/2 loops that eventually lead to sections with well-formed planar polar (PP) textures in a cylindrical capillary of radius R. (I) Pre-collision: ribbon shaped loops of vertical height $2y_\infty$=1.33R grow axially with the motion of branch points and shrinkage of the +1 linkage string. (II) Collision: Loop-loop merging with the formation of a double cusp of angle β and disclination curvature κ. Tension forces pinch the branch point. (III) Pinching and vertical line relaxation: curvature-driven motion. (IV) Formation of a single planar polar domain with two parallel +1/2 lines separated at $2y_\infty = 1.33R$. (V) Enlarged view of collision, junction formation, director fields, and junction angle β.

A number of key geometric characteristic of the loop-loop pre-collision stage (I) have been reported[10] due to the adaptive nature of the tension and bending stiffness of disclinations under confinement. According to Frank's disclination elasticity model the material length scale ℓ_m associated with the disclination and the defect-defect separation distance $2y_\infty$ are:[7-10]

$$\ell_m \equiv \frac{1}{\sqrt{a}} = \sqrt{\frac{k_c}{\gamma_{o,1/2}}} = \frac{1.68R}{\sqrt{\ln\left(\frac{\sqrt[5]{4}R}{2r_c}\right)}}, \quad y_\infty = \frac{R}{\sqrt[5]{4}} = 0.66R \tag{1}$$

where $a=\gamma_{o,1/2}/k_c$ is the ratio of tension to bending stiffness and r_c is the nano-scale disclination core radius. Using the Frank model (eqn.(1)) with $R/r_c \approx 1\times10^4$ and imposing the experimentally observed branch angle $\varphi \approx 60^o$, the numerical solution to the disclination elastica in the pre-collision stage (Figure 1(I))leads to the following scaling estimates at the branchpoint:[7-8]

$$\ell_m \approx \frac{R}{3},\ \kappa^* \approx \frac{10}{3R},\ \ell_m \cdot \kappa^* \approx \frac{10}{9},\ y_\infty \cdot \kappa^* \approx \frac{22}{10},\ \frac{\ell_m}{y_\infty} \approx \frac{1}{2} \tag{2}$$

where κ* is the disclination curvature at the two moving branch points (Fig.1(I)),showing that line stiffness responds to the confinement to yield $\kappa^* \approx 3.33/R,\ \beta \approx 60^o$, revealing a novel interaction between disclination line tension $\gamma_{o,1/2}$ and bending k_c and their adaptive nature.

The key issues addressed in this paper follow from a closer consideration of Figure 1.The branch points' collision (II) gives rise to a junction of four disclinations (II), locally equivalent to an intersection of two lines, characterized by a branch angle β and by the curvature κ (Fig.1(V)). Assuming geometric compatibility between (I,II), we would expect the lines' curvature atcollision (II) to reflect a balance of tension and bending forces acting on the lines while the vertical pinching of the junction should reflect how tension initiates the relaxation (III). Finally, the vertical relaxation (III) should be a curve shortening process driven by both tension and bending forces.

The dynamics of disclination line and relaxation stage (III) have been investigated previously. Figure 2 shows experimental data for a confined Sunset Set Yellow[11] solution. Compared to reported data for a bulk of nematic liquid crystal mixture E7[24], it can be seen the relaxation time is a function of materials properties and the geometry and it can vary from few seconds to few minutes. Also anchoring in a capillary affects the disclination shape. There are few theoretical studies of this phenomenon[24-26] which focus only on the tension of a disclination line. As we mentioned before, the bending energy plays an important role in nematic disclination dynamics and affects the relaxation time which is a key parameter in the design and operation of sensors and actuators. As we will show below, the disclination relaxation decays linearly (for tension only regime) and exponentially in time (by considering the bending effect).

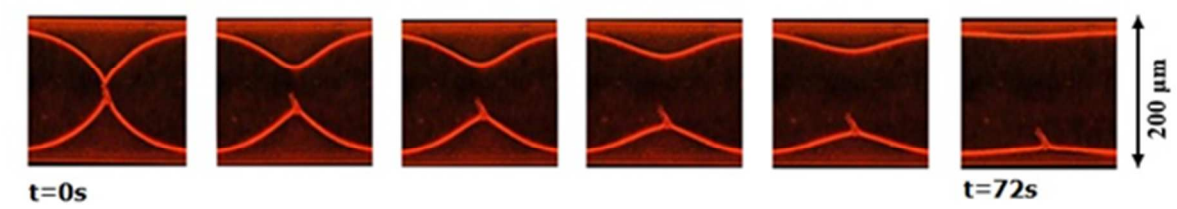

Figure 2. Relaxation of disclination lines in a confined SSY chromonic liquid crystal solution. The effect of wall surfaces leads to forming two straight +1/2 disclination lines (Adapted from Ref. 11).

The specific objectives of this paper are: (*i*) to use the disclination elastica model to describe the novel d*e*fect physics of loop-loop merging, junction point pinching, and relaxation under tension and bending forces of wide interest to defect structure and dynamics under confinement, and (*ii*) derive specific relations between the relaxing line geometry and nematic viscoelastic moduli. This paper builds on our previous work on nematic liquid crystals under capillary confinement.[7-10] Understanding how calibration of bending and tension controls

disclination geometry and kinematics will be useful to design new structures in LCs and disclination-based rheo-physics can be a practical characterization tool.

The organization of this paper is as follows. Section 2 presents the disclination geometry, the disclination elastica model, the method used to calculate the corresponding disclination space curves, and an analytical solution of the loop-loop collision/merging stage. Section 3 presents the collision, pinching, and relaxation stages and the procedure to estimate viscoelastic properties of nematics from defect relaxation that includes bending and tension elasticity. Section 4 presents the conclusions.

2. Disclination Elastica Model

2.1. Disclination Curves Geometry and Kinematics

Figure 3 shows the (x,y) coordinate system and geometry of a +1/2 disclination curves consisting of two planar m=+1/2 disclination curve evaluating to form tow well-formed m=+1/2 disclination lines. The collision point located at (x,y)=(0,0).

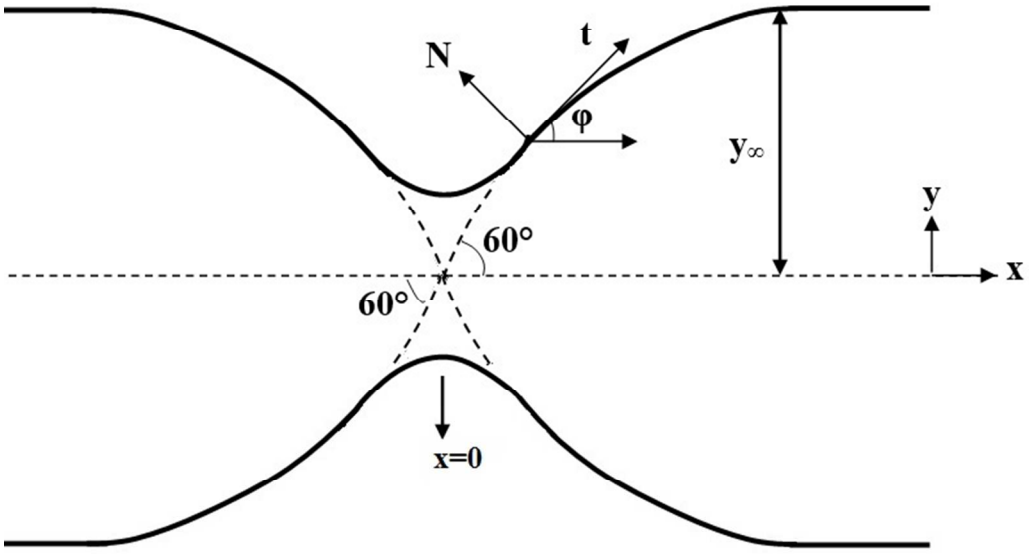

Figure 3. Schematic of the coordinate system and geometry of two m=+ ½ lines evaluating from the collision point at $x=0, y=0$. The x-axis is along the capillary axis. The angle between the x-axis and the tangent vector **t** is φ, **N** is the unit normal, and s the arc-length. The collision point angle, is 60°. y_∞ is the final defect distance[23] which is the half-separation distance between the two + ½ lines.

The unit tangent **t** and the unit normal **N** to the filament are given by:[7-9]

$$\mathbf{t}(s,t)=\frac{\partial \mathbf{r}(s,t)}{\partial s} \quad ; \quad \frac{\partial \mathbf{t}(s,t)}{\partial s}\equiv\frac{\partial^2 \mathbf{r}(s,t)}{\partial s^2}=\kappa\,\mathbf{N}(s,t) \qquad (3a,b)$$

where $\boldsymbol{\kappa}=\partial\mathbf{t}/\partial s$ is the curvature, **r** is the position vector and s the arc length, respectively. **t** is a unit vector which is expressed with the tangent angle φ(s): $\mathbf{t}(s)=(\cos\phi(s),-\sin\phi(s))$. The non-material line velocity **u** is:

$$\mathbf{u}=U(s,t)\mathbf{t}(s,t)+W(s,t)\mathbf{N}(s,t) \qquad (4)$$

where $U\mathbf{t}$ is the tangential velocity, and $W\mathbf{N}$ is the normal velocity. The evolution of the disclination curvature κ(s,t) and the metric g are:[27]

$$\frac{\partial \kappa}{\partial t} = W\kappa^2 + \frac{\partial^2 W}{\partial s^2} + U\frac{\partial \kappa}{\partial s}, \quad \frac{\partial g}{\partial t} = g\left(\frac{\partial U}{\partial s} - \kappa W\right) \tag{5a,b}$$

For a disclination line the only relevant velocity is W (U=0), the tangential force balance equation is satisfied for a constant line tension (see Appendix) and the metric obeys $\partial g / \partial t = -g\kappa W$ (line shrinkage).

2.2. Disclination Shape Equation

In this section, largely based on references [7-10] we derive the disclination shape equation by formulating the force balance equation due to internal and external stresses on the line. Internal stresses include line tension and line bending forces are derived using Frank elasticity. The shape equation is then used to formulate the disclination shape evolution.

The Frank gradient elasticity density *f* for uniaxial NLCs, using the one constant approximation is:[2]

$$f = \frac{K}{2}\left((\nabla \cdot \mathbf{n})^2 + (\nabla \times \mathbf{n})^2\right) \tag{6}$$

where $K=K_{11}=K_{33}\approx 10$ pN. It has been approved experimentally for nematic phase of a self-assembled lyotropic chromonic liquid crystal the elastic moduli of splay (K_{11}) and bend (K_{33}) are in the order of 10 pN while the twist modulus (K_{22}) is much smaller.[28] Saddle-splay K_{24} $\nabla.\left[(n.\nabla)n - (\nabla.n)n\right]$ is not considered because under assumptions and approximations of this first order planar (no torsion) model it plays no role. The assumptions and approximations are:

1. Disclinations are of the singular core Frank type, with the director locally normal to the line axis, exhibiting splay and bend deformations and no twist and no escape in the third dimension are considered (see Figure 3) ;

2. The core energy is neglected. The saddle-splay energy of + disclinations decreases the core tension but it is neglected as it is usually less than 10% of the retained director-bases tension. Finally the topological invariant associated with saddle-splay is conserved in a defect branching process and hence whether we have +1 of 2 +1/2 lines this line core effect will remain unaffected. .
3. Higher order curvature terms and curvature gradients are neglected.

In terms of textures, previous results are consistent with our assumptions. For PR configuration, a line singularity exists along the axis and K_{24} doesn't contribute to the director free energy.[29] For PP, the term is zero, so it is irrelevant for this configuration too. In general, for the case of strong anchoring, K_{24} doesn't have a major portion in equilibrium bulk energy but when escaped radial (ER) configuration becomes stable under weak anchoring, K_{24} should be considered.[29,30] For Sunset Yellow FCF chromonic liquid crystal, large value of K_{24} leads to ER configuration.[30]

Minimizing the total free energy results in the Euler-Lagrange equation:[31] $K\nabla^2\mathbf{n} = \lambda\mathbf{n}$; K is the Frank elastic constant, and λ is the Lagrange multiplier that takes into account the unit length restriction $\mathbf{n}\cdot\mathbf{n}=1$. By integrating eqn. (2) in a cylinder of radius *R,* one obtains the line tension $\gamma_o(PP)$ of a single straight *m*=+1/2 disclination in the PP texture:[32]

$$\gamma_{1/2} = \gamma_o(PP) = \gamma_{o,1/2} + \pi\sigma_c r_c^2; \quad \gamma_{o,1/2} = \frac{\pi K}{2}\left(\ln\left(\frac{R^2}{2r_c y_\infty}\right)\right) \tag{7}$$

where R_c is the capillary radius, r_c is the core radius, σ_c is the core energy density that is usually assumed to be negligible in comparison to the other terms. The total line energy $\gamma_{1/2}$ (energy/length) of a curved +1/2 disclination is given by the sum of the core energy $\pi\sigma_c r_c^2$, bare line tension $\gamma_{0,1/2}$,and the bending $k_c\kappa^2/2$ contributions:[7]

$$\gamma_{1/2} = \pi\sigma_c r_c^2 + \gamma_{0,1/2} + \frac{k_c}{2}\kappa^2;\ k_c = \frac{\pi K R_c^2}{\sqrt{2}} \qquad (8a,b)$$

where k_c is the bending modulus (energy × length) and only the leading order bending term is retained. The force balance equation represents the Rouse model, and it is written by the sum of line force $\nabla_\ell . \mathbf{T}$ and the surrounding medium viscous force:

$$\gamma_1 W \mathbf{N} = \nabla_\ell . \mathbf{T}$$

(9)

where **T** is the + ½ disclination line elastic stress tensor, $\nabla_\ell(\bullet) = \mathbf{t}\,\partial(\bullet)/\partial s$ is the line gradient operator, γ_1 is the rotational viscosity. To find the line elastic stress tensor **T**, we perform a variation of the total line elastic free energy due to tangential and normal displacements and find:[33] $\mathbf{T} = T\mathbf{tt} + B\mathbf{tN}; T = (\gamma_{1/2} - \mathbf{M} : \mathbf{b}); B = -\frac{\partial M}{\partial s}$

(10)

where $\gamma_{1/2}\mathbf{tt}$ is the thermodynamic tension stress analogous to 3D pressure. The elastic line stress **T** has a mechanical contributions ($-\mathbf{M} : \mathbf{b}$), since there can be no bending without tension; here **b** is the line curvature tensor given by $\mathbf{b} = \kappa\mathbf{tt}$. The last term in equation (6) are the bending stresses that arise under curvature gradients ($\partial\kappa/\partial s \neq 0$). The scalar moment M, line moment tensor **M**, and line elastic stress tensor $\mathbf{T}$ are:

$$M = k_c\kappa,\ \mathbf{M} = M\,\mathbf{tt}\ ;\ \mathbf{T} = \left(\gamma_{o,1/2} - \frac{k_c}{2}\kappa^2\right)\mathbf{tt} - k_c\frac{\partial\kappa}{\partial s}\mathbf{tN} \qquad (11a,b,c)$$

From eqns. (5) and (11) we find the governing equations under the U=0 gauge:

$$\gamma_1 W = \left(\gamma_o - \frac{k_c}{2}\kappa^2\right)\kappa - k_c\kappa_{ss},\quad \frac{\partial\kappa}{\partial t} = W\kappa^2 + \frac{\partial^2 W}{\partial s^2},\quad \frac{\partial g}{\partial t} = g(-\kappa W) \qquad (12a,b,c)$$

We use eqns.(11) for the collision, pinching and relaxation processes. The standard numerical integration of eqn.(11a) for W=0 , parametric data, boundary conditions and how to compute the disclination space curves y(x) from the curvature k(s) are found in [7].

2.2 Poleni's Curve

The Poleni curve is a single loop solution to Euler's elastic, that has been used to describe among other things the curvature of a steel saw blade under tension and liquid meniscus.[34]At the collision of two branch points (Figure II,V), the disclination curve can be obtained from the steady form of equation (10a):

$$\kappa_{ss} + \frac{\kappa^3}{2} - a\kappa = 0 \tag{13}$$

Here we introduce a closed form solution to eqn.(13) and the corresponding space curve (y(s), x(s))that fits the loop collision stage , first introduced in 1729 by Poleni:[20, 34]

$$\kappa(s) = \frac{2\sqrt{a}}{\cosh\left(\sqrt{a}s\right)} \rightarrow \sin\frac{\varphi}{2} = \operatorname{sech}\left(\sqrt{a}s\right) \xrightarrow{\text{space curve}} \begin{cases} x(s) = s - \dfrac{2}{\sqrt{a}}\tanh\left(\sqrt{a}s\right) \\ y(s) = \dfrac{2}{\sqrt{a}\cosh\left(\sqrt{a}s\right)} \end{cases} \tag{14}$$

where $x(0) = 0,\ x_s(0) = 1, y(0) = 2/\sqrt{a},\ y_s(0) = 0$ and φ is the tangent angle; see Figure 2.

This continuous curve contains an intersection at $S^* = 2\tanh\left(\sqrt{a}S^*\right)/\sqrt{a}$, which joins a cusp (lower region) with a loop (upper region). The bottom part of figure 4 shows a typical fit of Poleni's curve to the numerical solution to the elastic in the precollision stage, where each branch of each loop is computed by solving eqn.(8) with prescribed branch angle φ and $y_\infty = 0.665R$

.Figure 4(b) shows the curvature κ(s) pulse-like profile surrounding the cusp for micron range ℓ_m .The increasing curvature introduces bending energy that resists the pulling tension and gives rise to this single loop solution to the elastica.

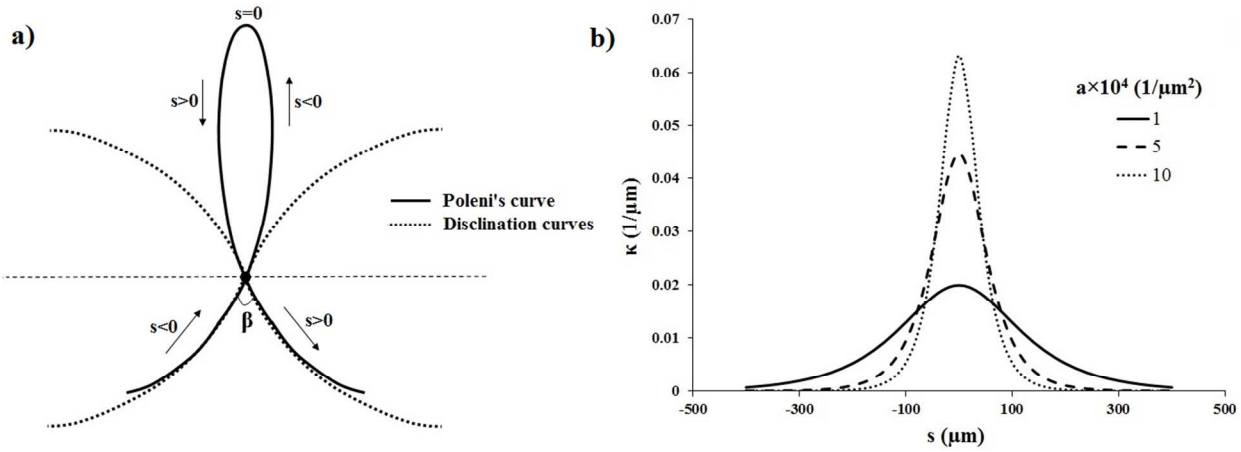

Figure 4. (a) Geometry and coordinates of Poleni's curve; **(b)** Curvature as a function of arc-length; from eqn.(14).

The predicted quantities for disclinations under confinement extracted from Poleni's elastica are: the aperture angle β, the disclination curvature at the intersection $\kappa(S^*)$, the asymptote y_∞ and their dependence on the material length scale ℓ_m and on the capillary confinement intensity R.

3. Results and Discussion

3.1. Collision Stage

In this section we describe the geometry of the unstable junction that leads to pinching and in the following section we use this geometry to calculate the forces that lead to the break-up. Superposing a Poleni curve and its reflection creates a double loop curve (Figure 5), where

each Poleni curve satisfies the elastica eqn.(11).We then attach the two Poleni curves ($s \le -S^*$, $s \ge S^*$) and remove the loops ($-S^* < s < S^*$), duplicating the unstable state at collision:

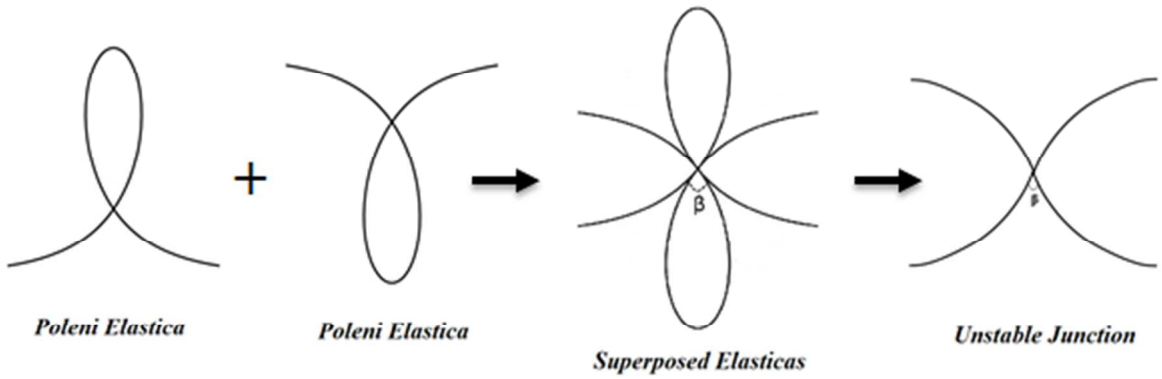

Figure 5. Superposing a Poleni curve and its reflection creates a double loop curve (superposed elasticas). Cutting the two loops gives the unstable junction that eventually pinches and allows a single loop formation. The junction angle β reflects the bending and tension forces.

The real junction will connect the loops with a nano-scale disclination point formed by the collision of the two branch points. We note that here we are only concerned with the geometry and stresses of the unconnected (superposed) Poleni curves.

From eqn.(13), x(S*)=0, we find the invariant $\sqrt{a}$ S*=S*/ℓ_m:

$$S^*/\ell_m = 2\tanh\left(S^*/\ell_m\right) = 1.915 \tag{15}$$

From the tangent angle φ in eqn.(13) $\left(\varphi = 2\sin^{-1}\left(\operatorname{sech}\left(s/\ell_m\right)\right)\right)$ and the S*/ℓ_m invariant, we find the invariant junction angle β :

$$\beta = 4\left(\pi - \sin^{-1}\left(\operatorname{sech}\left(S^*/\ell_m\right)\right)\right) = 56.5^0 \tag{16}$$

This unique angle is essentially equal to that computed previously (see ref.(7)) based for the pre-collision stage. Using Poleni's curvature from eqn.(14) and the invariant S^*/ℓ_m we find the maximum curvature at the junction:

$$\kappa(S^*) = \frac{2}{\ell_m \cosh\left(S^*/\ell_m\right)} = \frac{0.58}{\ell_m} \tag{17}$$

For $\beta = 56.5^0$, pre-collision computations give $\kappa(S^*) = 0.0164$. The junction height $y(S^*) \equiv y_\infty$ from the zero curvature asymptote found from eqn.(14) and the invariant S^*/ℓ_m is:

$$y(S^*) \equiv y_\infty = \ell_m \tag{18}$$

Combining eqns.(16 and 17) we find another invariant

$$\kappa(S^*) y_\infty = 0.58 \tag{19}$$

Table I summarizes the numerical pre-collision results extracted from [7-10] and the Polenis' elastic at collision. In the former we imposed $\varphi=60^0, y_\infty = 0.66R$ while in the later these are results from the model. The table shows that Poleni's analytical predictions are in very good agreement with pre-collision numerical calculations, especially in the intersection region as shown in Fig.(3a), demonstrating that the initial conditions (Poleni curve) is consistent with the numerical solutions of the pre-collision stage.

Table I. Geometry and material length scales estimates for numerical pre-collision (numerical [7-10]) and collision (Poleni curve predictions from eqns.(14-19)).

Stage	***Curvature***	***Angle***	***Material/geometry length scale ratio***	***Defect separation/geom.***	***Material/def. separation length scale***

				length scale ratio	***ratio***
Pre-collision (numerical)	$\kappa^* = \frac{3.33}{R}$	$\varphi_{bp} = 60^o$	$\ell_m \cdot \kappa^* \approx 1.1$	$y_\infty \cdot \kappa^* \approx 2.2$	$y_\infty / \ell_m \approx 2$
Collision (Poleni)	$\kappa(S^*) = 1.64 / R$	$\beta(S^*) = 56.6^o$	$\ell_m \cdot \kappa(S^*) = 0.58$	$\kappa(S^*) y_\infty = 1.1$	$y_\infty / \ell_m \approx 2$

Next we briefly discuss the energies and stresses associated with the cusp that remains after removing the loop. After removing the loop, the scaled scalar tension and bending stresses (eqns.(11)) acting on each disclination piece at s=S* are:

$$T/\gamma_{o,1/2} = \left(1 - \frac{\ell_m^2 \kappa^2}{2}\right) = 1 - \frac{(0.58)^2}{2} = 0.83$$

$$B/\gamma_{o,1/2} = -\ell_m^2 \frac{d\kappa}{ds} = -\ell_m \kappa \tanh\left(\sqrt{a}s\right) = \frac{\ell_m^2 \kappa^2}{2}\sqrt{\frac{4}{\ell_m^2 \kappa^2} - 1} = 0.55 \qquad (20)$$

and $T/B = f(\ell_m^2 \kappa^2) = 1.50$. Removing these stress loads at the junction will lead to the pinching instability.

The dimensionless elastic energy density $e/\gamma_{0,1/2}$ of the disclination cusp is a shifted hyperbolic secant square:

$$\frac{e}{\gamma_{0,1/2}} = 1 + 2\,\mathrm{sech}^2\left(\sqrt{a}s\right) \qquad (21a,b)$$

which is a single hump curve with maximum at s=0.At the junction (s=S*) bending is 1/3 times tension and then it decreases towards zero. Next we delete the loop ($-S^* \le s \le S^*$) and retain the

cusp of a Poleni curve. Figure 6 shows the dimensionless tension and bending elasticity ($2\,\mathrm{sech}^2\left(\sqrt{a}s\right)$) as function of "x", showing the bending energy cusp.

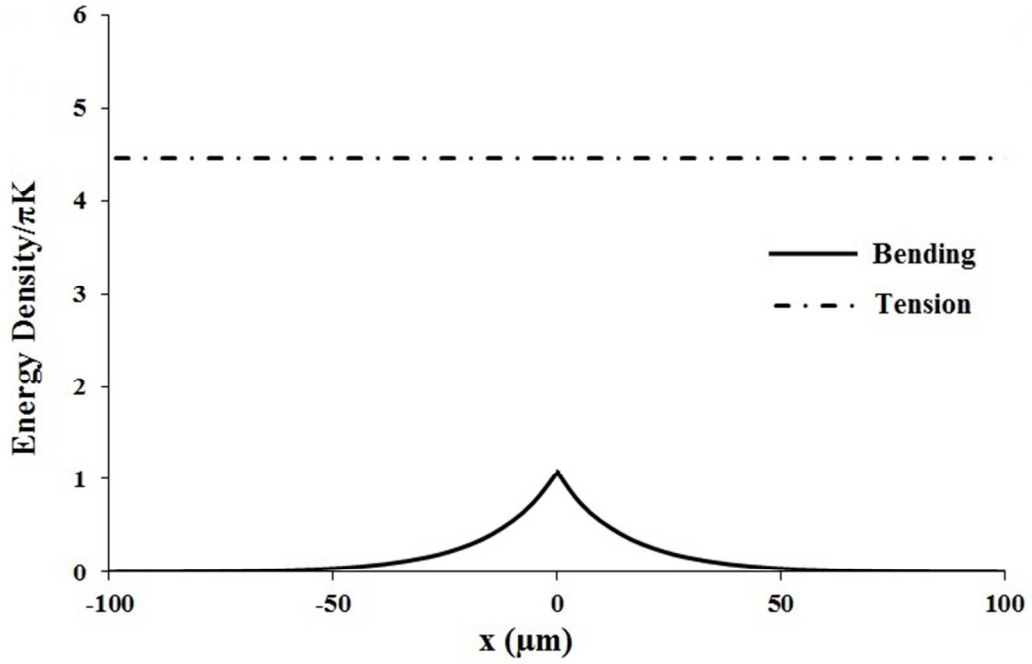

Figure 6. Dimensionless bending energy density as a function of distance x.

The net energy difference $E_{Poleni} - E_{PP}$ between the two Poleni's curves and the planar polar texture that drives the relaxation is:

$$E_{Poleni} - E_{PP} = 4\gamma_{0,1/2}\left\{\left(\int_0^L \frac{1}{\cos\varphi}dx - L\right) + 4\left(\int_0^L \frac{\mathrm{sech}^2\left(\sqrt{a}s(x)\right)}{\cos\varphi}dx\right)\right\} \quad (22)$$

Where L is of the order of the capillary radius R. The tension driving force is due to line length decrease and the bending driving force is due to the curvature.

3.2. Pinching

The pinching process (Fig.7(b)) that follows collision of the two branch points can be viewed as a form of frustrated T1 topological process found in foams, networks, and cellular patterns.[35] In the pre-collision stage the +1 disclination line to joins +1/2 loops shrinks to a isotropic junction point, but instead of stretching as T1 process, it pinches creating a larger +1/2 loop; see Fig.(1).

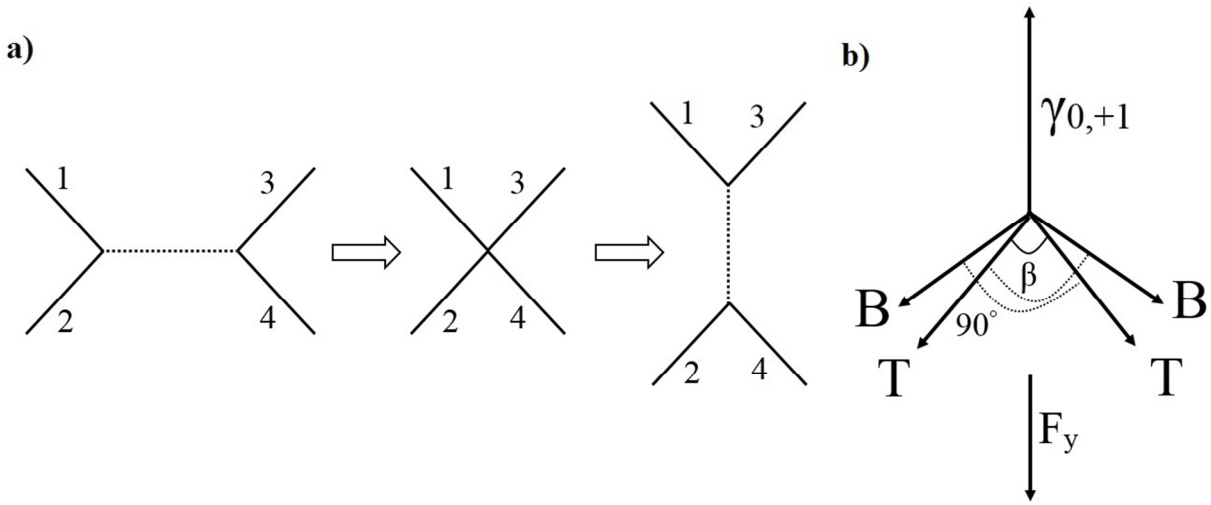

Figure 7.**(a)** Neighbor exchange (T1) process (Adapted from ref. 36). **(b)**The pinching process. The dotted lines represent the 90° angle between the tension T and bending B forces. A net vertical force due to tension (T) and bending (B) overcomes a resistance associated with the junction here represented by a +1 line.

We perform a force balance equation around the branch point. The control volume is a short +1 disclination cylinder of length $2r_c$ with semi-circular ends, and diameter $2r_c$; here r_c is the characteristic nanoscale radius of a disclination. The cylinder axis is along the y-axis. Halving the control volume and considering the bottom half, the net acting force **F** is:

$$\mathbf{F} = \hat{\boldsymbol{\delta}}_y \cdot \mathbf{T}_{+1} + \sum_{i=1}^{2} \mathbf{t}^i : \mathbf{T}^i_{+1/2} \qquad (23)$$

where $\hat{\boldsymbol{\delta}}_y$ is the unit vector in the vertical y-direction, $\mathbf{T}_{+1}$ is the stress in the +1 junction, $\mathbf{t}^i$ is the i^{th} unit tangent vector to the +1/2 lines, and $\mathbf{T}^i_{+1/2}; \{i=1,2\}$ are the line stress tensor of the +1/2 lines. Using eqn. (9c) these stress tensors are:

$$\hat{\boldsymbol{\delta}}_y \cdot \mathbf{T}_{+1} = \gamma_{o,1}\hat{\boldsymbol{\delta}}_y \equiv \pi K \ln\left(\frac{R}{r_c}\right)\hat{\boldsymbol{\delta}}_y;\ \ \mathbf{t}^i \cdot \mathbf{T}^i_{1/2} = T^i\mathbf{t}^i + B^i\mathbf{N}^i; i=1,2 \tag{24}$$

where we assumed a pure tension on the +1 line , and where T^i, B^i are given in eqn.(20); the standard expression for $\gamma_{o,1}$ is found in [2]. Projecting eqn. (23) along the vertical (y-direction) we find the net downward force F_y at the junction:

$$\begin{aligned} &F_y = \gamma_{o,1} - 2B\left|\mathbf{N}^i \cdot \hat{\boldsymbol{\delta}}_y\right| - 2T\left|\mathbf{t}^i \cdot \hat{\boldsymbol{\delta}}_y\right| = \gamma_{o,1} - \sqrt{3}\left(B+T\right) = \gamma_{o,1} - 3.6\gamma_{o,1/2} \approx 50K \\ &\left|\mathbf{N}^i \cdot \hat{\boldsymbol{\delta}}_y\right| = \left|\mathbf{t}^i \cdot \hat{\boldsymbol{\delta}}_y\right| = \sqrt{3}/3 \end{aligned} \tag{25}$$

where we used Poleni's curve predictions (eqns.(14)). Using R=100 μm and r_c=10nm, we find a net downward force of the order of Fy≈-50K, where K is the Frank elastic constant. The downward force from the bottom section and the corresponding upward force from the top section pinch the junction and complete the single loop formation.

3.3 Relaxation

We analyze the late stage regime of the relaxation given by the linearized version equation (12) obtained by neglecting $k_c\kappa^3/2$ and assuming a constant metric g (eqn.(5)):

$$\gamma_1 W = \gamma_o \boldsymbol{\kappa} - k_c \boldsymbol{\kappa}_{xx},\quad \frac{\partial \boldsymbol{\kappa}}{\partial t} = \frac{\partial^2 W}{\partial x^2} \tag{26a,b}$$

Assuming that in a (x, y) frame, the disclination's shape is described by a curve y=H(x,t), and $H_x \equiv \partial H/\partial x$ is sufficiently small, then the normal velocity W and curvature κ are: $W=\partial H/\partial t$, $\kappa = H_{xx}$ and the disclination shape equation (26a) becomes:

$$\frac{\partial H}{\partial t} = D_\ell \frac{\partial^2 H}{\partial x^2} - \delta \frac{\partial^4 H}{\partial x^4} \tag{27}$$

where $D_\ell = \gamma_{o,1/2}/\gamma_1$ is the line diffusivity and $\delta = k_c/\gamma_1$. For m=+ ½ disclinations, the tension $\gamma_{o,1/2}$ and bending k_c moduli are given in equations (6b and 6c). The solution of the relaxing shape around the collision point (x=0) is

$$H = H_\infty + (R - H_\infty) e^{-t/\tau} \cos \lambda x, \quad \frac{1}{\tau} = D_\ell \left(\lambda^2 + \lambda^4 . \ell_m^2 \right) \tag{28}$$

where τ is the disclination relaxation time. It can be seen by ignoring the bending term, the relaxation decays linearly in time as found previously.[22] Assuming a decay vector $\lambda = \pi/4R$, where R is the characteristic geometric scale (capillary radius R), the relaxation rate τ is given by the line diffusion term ℓ_{ex}^2/D_ℓ times the length scale factor $1/\left(1+\left(\ell_m/\ell_{ex}\right)^2\right)$:

$$\tau = \frac{\ell_{ex}^2}{D_\ell}\left(1+\left(\frac{\ell_m}{\ell_{ex}}\right)^2\right)^{-1} \tag{29}$$

where $\ell_{ex} = 4R/\pi$ is the external length scale.

Based on figures 3 and 4, we see the maximum in y(x) curve at the center where the collision happens. Then the curvature decreases to zero at the point of inflection. Over time, because the

disclination curve relaxes to a straight line as a results of bending stiffness, the maximum curvature goes to zero.

3.4 Viscoelastic Properties

The loop-loop coalescence model can be used to approximate viscoelastic properties such as rotational diffusivity, the average Frank elastic constant. Using the Frank disclination model ($\ell_m = R/3$) and eqn.(29) we find :

$$\tau \approx \frac{R^2}{5D_\ell} \tag{30}$$

Hence measuring τ gives the line diffusivity $D_\ell = \gamma_{o,1/2}/\gamma_1$ and the elastic bending/viscous rotation ratio: $\ell_m^2 D_\ell = k_c/\gamma_1$. Using the Frank dislination model (eqn.(7) for $\gamma_{o,1/2}$) we then find the rotational viscosity $\gamma_1 = \gamma_{o,1/2}/D_\ell$. This value can be tested by using different capillary radii to show that it is essentially independent of R.

As an initial application of the property determination procedure. Using experimental data (Ref. 11) for ℓ_{ex}=100μm, the measured relaxation time is τ= 72s, and from Frank's model with K=10 pN, $l_m \approx 30$ μm. Using eqn.(29) we find $D_\ell = \gamma_0/\gamma_1 \approx 2.77\times10^{-11} m^2/s$ and $k_c/\gamma_1 = \ell_{in}^2 D_\ell \approx 3.5\times10^{-20} m^4/s$. With these values the rotational viscosity is $\gamma_1 = \gamma_{0,1/2}/D_\ell = 3.91\, Pa.s$, which compares well with other reported values for the same liquid crystal.[26, 37]

3.5. Model extension

Here we briefly discuss a few significant possible extensions and generalizations of the planar elastica model and its applications in the absence of external fields.

(i) Capillaries with complex cross-sections: the confinement cross-sectional geometry affects the defect formation. For example, nematics confined in elliptic cylinders with homeotropic anchoring can show escaped-radial configuration for micro-meter size;[38] in this case the nematic elastica should include the neglected saddle-splay. The confinement cross-section can be designed to incorporate stable +1 defects by immersing micro fibers in a confined nematic [39]; in this case the PP-PR transformation is frustrated and branch points remain static.

(ii) Polygonal capillaries: under strong homeotropic anchoring the strength m_N of bulk defects in nematics inside polygonal capillaries of N sides obey Zimmer's rule [40,41]:

$$m_N = \frac{N-2}{2} \tag{31}$$

with the defect core type following an odd-even rule: odd N yield singular and even N yield non-singular cores. For odd polygons (N=5,7…) possible branching phenomena that obey Kirchhoff defect branching[7,42], and Zimmer's rules are:

$$+\frac{(N-2)}{2} \rightarrow (N-2)\left(+\frac{1}{2}\right) \tag{32}$$

For even polygons the cores are non-singular and saddle splay needs to be included.

(iii) Non-planar elastica: non-planar disclinations are described by curvature and torsion and hence Frank anisotropies and saddle-splay need to be retained. Disclination double helices or

disclination DNA are observed in chiral nematics.[43] Single low tension helical disclination around a high tension straight disclination are observed also in chiral nematics.[44]

4. Conclusions

This paper presents theory, scaling and analysis of disclination loop-loop collision and relaxationthat appears in the transformation of a nematic liquid crystal planar radial texture with one axial +1 singular disclination into a planar polar texture with two +1/2 singular disclinations in a cylindrical capillary whose surfaces impose strong homeotropic anchoring. The defect process has three stages: (i) loop-loop collision, (ii) pinching, and (iii) time relaxation into a larger single loop, described by a Rouse-Frank model. The geometry of loop defects are simulated with the disclination elastica model based on Frank elasticity and the dynamics with a Rouse model. In this model disclination have both tension and bending stiffness whose magnitude depends on the degree of confinement or capillary radius R. The disclination elastic is identical to the Euler elastic. The disclination shapes involved in the loop-loop merging are well described by the Poleni curve which is a non-periodic single-loop solution to Euler's elastic. Loop-loop merging give rise to a two line intersection whose angle is close to 60^{o} which is an invariant of the Poleni curve. The curvature at the intersection is also expressed as a Poleni invariant. These results for loop-loop collision are the used to demonstrate that pinching the two line intersection is due to tension overcoming bending. The excess energy of the curved lines with respect to the planar polar texture drives the relaxation here described by a linear Rouse model, yielding a close-from expression of the longest relaxation time in terms of the disclination line diffusivity, the confinement, and the ratio of tension-to-bending stiffness. The combined Rouse-Frank model is used to formulate a procedure to predict the average Frank elasticity and the rotational viscosity of nematic liquid crystals. The nematic elastica model used

to solve texture transformations under confinement can in the future be extended to non-planar disclinations where disclination torsion arises. The modeling predictions from the nematic elastica model enhance the current fundamental understanding of defect physics of liquid crystals.

Acknowledgements

This work is supported by a grant from the U.S. Office of Basic Energy Sciences, Department of Energy; grant DE-SC0001412.

References

1. M. Kleman and O.D. Lavrentovich, *Soft Matter Physics*, Springer-Verlag, New York, 2003.

2. P. G. de Gennes, *The Physics of Liquid Crystals*, Oxford University Press, New York, 1995.

3. E.G. Virga, *Variational Theories for Liquid Crystals*, Chapman Hall, London, 1994.

4. I. W. Stewart, *The static and dynamic continuum theory of liquid crystals: a mathematical introduction*, CRC Press, 2004.

5. O. D. Lavrentovich, P. Pasini, C. Zannoni, and S. Zumer, *Defects in Liquid Crystals, Nato Science Series, II. Matehamtics, Physics and Chemsitry*, Vol. 43. Kluwer Academic Publishers, Netherlands, 2001.

6. G. P. Crawford and S. Zumer, Eds. *Liquid Crystals in Complex Geometries: Formed by Polymer and Porous Networks*, Taylor & Francis, London, 1996.

7. A. Shams, X. Yao, J. O. Park, M. Srinivasarao and A. D. Rey, *Soft Matter*, 2012, **8**, 11135−11143.

8. A. Shams, X. Yao, J. O. Park, M. Srinivasarao and A. D. Rey, *Liq. Cryst.* 2015, **42(4)**, 506−519.

9. A. Shams, X. Yao, J. O. Park, M. Srinivasarao and A. D. Rey, *Soft Matter,* 2014,**10**, 3245−3258.

10. A. Shams, X. Yao, J. O. Park, M. Srinivasarao and A. D. Rey, *Phys. Rev. E*, 2014,**90(4)**, 042501**.**

11. X. Yao, Studies on lyotropicchromonic liquid crystals in nematic and biphasic regions, PhD Thesis, Georgia Institute of Technology, December 2011.

12. A. D. Rey, *Soft Matter*, 2010, **6(5)**, 3402−3429; A.D. Rey, *Soft Matter*, 2007**2**, 1349−1368.

13. B. Wincure and A.D. Rey, *Liq. Cryst.*, 2007, **34(12)**, 1397−1413; *Continuous Mechanics and Thermodynamics*, 2007, **19**, 37−47; *J. Chem. Phys*., 2006,**124**, 244902.

14. Y. K. Kim, S. V. Shiyanovskii and O. D. Lavrentovich, *J. Phys.: Condens. Matter*, 2013, **25** 404202.

15. J. Gunther, E. L. Thomas, S. Clingman and C. K. Ober, *Polymer*, 1998, 39(19), 4497–4503.

16. M. Srinivasarao, in *Liquid Crystals In The Nineties And Beyond* , S. Kumar editor, 18-19,377-434, World Scientific, Singapore, 1995.

17- A. D. Rey, *Macromol. Theory Simul.*, 2002,**11(9)**, 944-952; *Langmuir*, 2003,**19**, 3677−3685; *Soft Matter*, **2**, 1349−1368, 2007; *Rheology Reviews 2008*, 2009, 71−135.

18. G. de Luca and A. D. Rey, *J. Chem. Phys.*, 2007,**126**, 094907; 2007,**127**, 104902.

19. R. B. Meyer, F. Lonberg, V. Taratuta, S. Fraden, S.-D. Lee and A. J. Hurd, *Faraday Discuss. Chem. Soc.*, 1985, **79**, 125–132.

20. T. Hangan, C. M. Murea and T. Sari, *Rendiconti del Seminario Matematico, SeminarioMatematico*, 2009, **67**, 59-76.

21. R. Levien, The elastica: a mathematical history, EECS Department, University of California, Berkeley, Technical Report No. UCB/EECS-2008-103, August 23, 2008.

22. P. M. Chaikin, T. C. Lubensky, *Principles of Condensed Matter Physics*, Cambridge University Press, Cambridge, 1995.

23. J. Yan and A. D. Rey, *Phys. Rev. E*, 2002,**65**, 031713; J. Yan and A. D. Rey, *Carbon*, 2003,**41**, 105–121.

24. N. Osterman, J. Kotar, E. M. Terentjev and P. Cicuta, *Phys. Rev. E*, 2010,**81**, 061701.

25. H. Imura and K. Okano, *Phys. Lett. A,* 1973, **42**, 403–404.

26. G. Ryskin and M. Kremenetsky, *Phys. Rev. Lett.* 1991, **67**, 1574–1577.

27. L. M. Pismen, *Patterns and Interfaces in Dissipative Dynamics*, Springer, 2006.

28. S. Zhou, K. Neupane,Y. A. Nastishin, A. R. Baldwin, S. V. Shiyanovskii, O. D. Lavrentovich and S. Sprunt, *Soft Matter,* 2014,**10**, 6571−6581.

29. D. W. Allender, G. P. Crawford, and W. Doane, *Phys. Rev. Lett.* 1991, 67, 1442–1445.

30. Z. S. Davidson, L. Kang, J. Jeong, T. Still, P. J. Collings, T. C. Lubensky, and A. G. Yodh, *cond-mat.soft*, arXiv:1504.03619v1, 14 Apr 2015, 1–6.

31. S. Chandrasekhar F.R.S. Liquid Crystals, 2 edition, Cambridge University Press, Cambridge, 1993.

32. M. E. Gurtin, *Thermomechanics of Evolving Phase Boundaries in the Plane*, Oxford University Press, New York, 1993.

33. A. Ludu, Nonlinear *Waves and Solitons on Contours and Closed Surfaces*, Springer-Verlag: Berlin, 2007.

34. G. Poleni, *Epistolarum Mathematicarum fasciculus*, Nabu Press (USA), 2012, ISBN 10: 1279951214 .

35. M. R. Kamal, T. A. O. Huang, and A. D. Rey. *J. Mater. Sci*. 1997, **32(15),** 4085-4099.

36. G. Schliecker, *Adv. Phys*., 2002, **51(5)**, 1319–1378.

37. H. Kneppe, F. Schneider and N. K. Sharma, *J Chem. Phys*. 1982, **77**, 3203-3208.

38. J. Jeong and M. W. Kim, App. Phys. Lett. 2012, **101,** 061914.

39. M. Nikkhou, M. Škarabot and I. Muševič, *Eur. Phys. J. E*. 2015, **38**, 23.

40. J. E. Zimmer and R. L. Weitz, in Extended Abstracts, 16th Biennial Conference on Carbon (American Carbon Society, San Diego, CA, 1983), p. 92.

41. G. Gupta and A.D. Rey, *Phys. Rev. Letters*, 2005, 95(12), 127805.

42. G. H. Yang, H. Zhang, L. J. Tian, Y. S. Wang, Y. S. Duan, *Commun. Theor. Phys*. (Beijing, China) 2005, **44**, 213.

43. P.E. Cladis, A.E. White, and W.F. Brinkmann, *J de Physique*, 1979, **40**, 325.

44. J. Rault, *Sol. State Comunn*. 1971, **9**, 1965.

Appendix

Here we show that the form of stress tensor (eqn.(11c)) is consistent with the kinematics in eqn.(9). The motion of a defect due to changes in **Q** is:

$$\frac{\partial \mathbf{Q}}{\partial t} = \mathbf{V} \cdot \nabla \mathbf{Q} \qquad \text{(A1)}$$

where **Q** is the symmetric traceless tensor order parameter and the **V** is the velocity vector. At the defect core axis, the shape of **Q+I/3** is that of an uniaxial oblate ellipsoid [13, 18]; **I** is the unit tensor. The unique axis of **Q** is **t** and on the plane perpendicular to **t** we have circular symmetry and the eigenvalues of **Q** only vary in radial direction perpendicular to **t**. Hence

$$\frac{\partial \mathbf{Q}}{\partial t} = \mathbf{V} \cdot \nabla \mathbf{Q} = W \frac{\partial \mathbf{Q}}{\partial z} \qquad \text{(A2)}$$

where z is a coordinate along **N** and W is the normal speed. Equation (A2) shows that $\partial \mathbf{Q} / \partial t$ depends only on the normal velocity of the disclination line. This fact is compatible with our stress tensor. We rewrite equation (8) as:

$$\mathbf{T} = \left(\gamma_o - \frac{k_c}{2} \kappa^2 \right) \mathbf{tt} - k_c \frac{\partial \kappa}{\partial s} \mathbf{tN} \qquad \text{(A3)}$$

The stress line gradient is:

$$\nabla_\ell \cdot \mathbf{T} = \mathbf{t} \cdot \frac{\partial \mathbf{T}}{\partial s} \tag{A4}$$

where ∇_ℓ is the line gradient. Using (A3) we find the vector line force:

$$\frac{\partial \mathbf{T}}{\partial s} = \left(-k_c \kappa \kappa_s\right)\mathbf{tt} + \left(\gamma_o - \frac{k_c}{2}\kappa^2\right)\kappa \mathbf{Nt} + \left(\gamma_o - \frac{k_c}{2}\kappa^2\right)\kappa \mathbf{tN} -$$

$$-k_c \kappa_{ss}\mathbf{tN} - k_c \frac{\partial \kappa}{\partial s}\kappa \mathbf{NN} + k_c \frac{\partial \kappa}{\partial s}\kappa \mathbf{tt} \tag{A5}$$

Replacing eq. (A5) in (A4) gives:

$$\nabla_\ell \cdot \mathbf{T} = \mathbf{t} \cdot \frac{\partial \mathbf{T}}{\partial s} = \left(-k_c \kappa \frac{\partial \kappa}{\partial s}\right)\mathbf{t} \cdot \mathbf{tt} + \left(\gamma_o - \frac{k_c}{2}\kappa^2\right)\kappa \mathbf{t} \cdot \mathbf{Nt} + \left(\gamma_o - \frac{k_c}{2}\kappa^2\right)\kappa \mathbf{t} \cdot \mathbf{tN}$$

$$-k_c \kappa_{ss}\mathbf{t} \cdot \mathbf{tN} - k_c \frac{\partial \kappa}{\partial s}\kappa \mathbf{t} \cdot \mathbf{NN} + k_c \frac{\partial \kappa}{\partial s}\kappa \mathbf{t} \cdot \mathbf{tt} = \tag{A6}$$

$$= \left(\left(-k_c \kappa \frac{\partial \kappa}{\partial s}\right) + k_c \kappa \frac{\partial \kappa}{\partial s}\right)\mathbf{t} + \left(\left(\gamma_o - \frac{k_c}{2}\kappa^2\right)\kappa - k_c \kappa_{ss}\right)\mathbf{N} = \left(\left(\gamma_o - \frac{k_c}{2}\kappa^2\right)\kappa - k_c \kappa_{ss}\right)\mathbf{N}$$

The general Rouse model reads [23]:

$$\nabla_\ell \cdot \mathbf{T} = \gamma_1 U(s,t)\mathbf{t}(s,t) + \gamma_1 W(s,t)\mathbf{N}(s,t) \tag{A7}$$

where γ_1 is rotational viscosity. On the tangential and normal directions we have

$$\nabla_\ell \cdot \mathbf{T} : \mathbf{tt} = \gamma_1 U;\ \nabla_\ell \cdot \mathbf{T} : \mathbf{NN} = \gamma_1 W \tag{A8 a,b}$$

From equation (A6):

$$\frac{\partial \mathbf{T}}{\partial s} : \mathbf{tt} = \left(-k_c \kappa \frac{\partial \kappa}{\partial s} \right) + \left(k_c \kappa \frac{\partial \kappa}{\partial s} \right) \equiv 0 \qquad \text{(A9)}$$

and

$$\left(\nabla_\ell \cdot \mathbf{T}_\ell \right) \cdot \mathbf{t} = \gamma_1 U = 0 \qquad \text{(A10)}$$

which is consistent with (A2).